The Astrophysical Journal, 995:120 (13pp), 2025 December 10 https://doi.org/10.3847/1538-4357/ae0fff

Long-term Monitoring of Scintillation in the Pulsar J0332+5434

Grayce C. Brown[1,2,10], Sofia Z. Sheikh[1,2], Luigi F. Cruz[1,2], Wael Farah[1,2], Vishal Gajjar[1,2], Christian Gilbertson[3], Brandon Grimaldo[1,2], Michael T. Lam[1,4,5], Sofia L. Marquez[1,2], Maura McLaughlin[6], Alexander W. Pollak[1,2], Andrew Siemion[1,2,7,8,9], and Gurmehar Singh[1]
[1] SETI Institute, Mountain View, CA 94043, USA
[2] Berkeley SETI Research Center, Berkeley, CA 94720, USA
[3] Center for Computing Research, Sandia National Laboratories, Albuquerque, NM 87185, USA
[4] School of Physics and Astronomy, Rochester Institute of Technology, Rochester, NY 14623, USA
[5] Laboratory for Multiwavelength Astrophysics, Rochester Institute of Technology, Rochester, NY 14623, USA
[6] Department of Physics and Astronomy, West Virginia University, Morgantown, WV 26501, USA
[7] Astrophysics, Department of Physics, University of Oxford, Keble Road, Oxford OX1 3RH, UK
[8] Jodrell Bank Centre for Astrophysics, Department of Physics and Astronomy, Alan Turing Building, University of Manchester, Oxford Road, M13 9PL, UK
[9] University of Malta, Institute of Space Sciences and Astronomy, Msida, MSD2080, Malta
Received 2025 January 9; revised 2025 September 29; accepted 2025 October 2; published 2025 December 10

Abstract

Changes in a pulsar's scintillation characteristics over time can be a useful way to probe the properties of the interstellar medium. Monitoring the scintillation bandwidth can be useful for correcting for scattering delay in pulse arrival time, which could be a significant source of error for precision pulsar timing projects. To better understand the magnitude and trend of scintillation bandwidth changes over long timescales (months–years), we performed long-term monitoring of PSR J0332+5434 with the Allen Telescope Array at radio frequencies ranging from 900 to 1956 MHz. In total, we collected more than 300 observations of PSR J0332+5434 over the course of 10 months, with observations taken daily to weekly. We find a mean scintillation bandwidth of 2.6 MHz (scattering delay of 0.06 μs) with a standard deviation of 1.3 MHz (0.03 μs) at 1140 MHz and a mean of 14.7 MHz (0.011 μs) with a standard deviation of 9.1 MHz (0.006 μs) at 1668 MHz. We see significant change over time on a timescale of ~200 days, suggesting that, for pulsars that are timed with submicrosecond precision, correcting for similar changes over time will be vital. We find no evidence for periodicity in the scattering delays. We describe a novel method for measuring the scaling index and compare it to established methods. We find the mean scintillation bandwidth frequency scaling goes as $\nu^{3.1 \pm 1.0}$.

Unified Astronomy Thesaurus concepts: Pulsars (1306); Radio pulsars (1353); Radio astronomy (1338); Radio telescopes (1360); Interstellar medium (847); Interstellar scattering (854); Interstellar scintillation (855); Observational astronomy (1145)

1. Introduction

Pulsars—rotating neutron stars that emit radiation from their poles—have extremely regular spin periods due to their high density and energy. Millisecond pulsars (MSPs), with periods on the order of milliseconds, have periods P and period derivatives $\dot{P}$ that have been measured with extreme precision; M. F. Alam et al. (2021) and G. Agazie et al. (2023a) measure changes in pulsar spin period with sub-μs accuracy. Discrepancies between the actual and predicted pulse arrival time could indicate a change in the light's path length, a technique that pulsar timing array (PTA) experiments have used to detect low-frequency gravitational waves (G. Agazie et al. 2023b).

Measuring these subtle changes in pulse arrival time to detect gravitational waves requires accounting for noise with sub-μs precision. One source of noise is the delay of pulse arrival and broadening of the pulse caused by interstellar scattering (ISS). This scattering delay is caused by a turbulent mix of free electrons whose density and velocity are changing chaotically along the line of sight (e.g., R. Narayan 1992). As a pulsar's radio emission travels through the interstellar medium (ISM), this turbulence causes refractive index fluctuations that lead to interference patterns, or spatial variations of intensity across the observer plane called scintillation. These interference patterns change if there are relative transverse motions between the source pulsar, the ISM, and the observer on Earth—for example, as Earth orbits the Sun (e.g., Y. Liu et al. 2023). The projection of these interference patterns across the observer plane cause variations in brightness across frequency and time, with the interference maxima being referred to as "scintles." As scattering along the line of sight changes with the motions of Earth, the ISM, and the pulsar, the size of these scintles can vary significantly from static model predictions (e.g., S. Sheikh et al. 2024).

Scintillation in the frequency domain can be characterized by its scintillation bandwidth, $\Delta\nu_d$, sometimes called the decorrelation bandwidth, which is traditionally taken as the half width at half maximum (HWHM) of the scintles on the frequency axis. One can also measure the scintillation timescale (distinct from the abovementioned timing delay), which is taken to be the half width at e^{-1} of the maximum of the scintles in the time domain. This paper will focus on the frequency domain and the scintillation bandwidth $\Delta\nu_d$, which relates to the scattering delay by the uncertainty relation

$$C_1 = 2\pi\tau_d\Delta\nu_d, \quad (1)$$

where τ_d is the scattering time delay, $\Delta\nu_d$ is the scintillation bandwidth, and C_1 is a factor of ~1–2 that depends on the

[10] Corresponding author.

wavenumber and geometry of the electron density spectrum (J. M. Cordes & B. J. Rickett 1998). For example, use of a thin-screen model with Kolmogorov scaling (A. Kolmogorov 1941) implies $C_1 = 0.957$ (J. M. Cordes & B. J. Rickett 1998); however, we will set $C_1 = 1$ as in L. Levin et al. (2016) and J. E. Turner et al. (2021) to be compatible with current literature.

There are two scattering regimes in the ISM: diffractive interstellar scintillation (DISS) and refractive interstellar scintillation (RISS). DISS causes the scintillation patterns that can be discerned on the timescale of a single observation. The interstellar turbulence that causes DISS can be described with a power-law wavenumber spectrum with the form

$$P_{\delta n_e}(q) = C_n^2 q^{-\beta}, \quad q_0 \leqslant q \leqslant q_1, \tag{2}$$

where C_n^2 is a constant that depends on where scattering occurs and can be determined by observables if β (the power-law index, J. M. Cordes et al. 1985) is assumed, where q_0 and q_1 are the wavenumber cutoffs. One common way to model and predict the effects of DISS is to use a thin-screen approximation—where the scattering occurs at a single location between the observer and the pulsar (P. A. G. Scheuer 1968)—paired with a model for the turbulence in the ISM, such as Kolmogorov turbulence ($x = 5/3$)[11] or a "square-law" structure function ($x = 2$). β relates to x via the relation

$$x = \beta - 2 \text{ for } \beta < 4, \quad x = 2 \text{ for } \beta > 4, \tag{3}$$

(J. M. Cordes & B. J. Rickett 1998) where x is the slope of the frequency-dependent scaling. The scintillation bandwidth $\Delta\nu_d$ scales with frequency by

$$\Delta\nu_d \propto \nu^{\alpha}, \quad \alpha = \frac{2\beta}{(\beta - 2)}, \tag{4}$$

where ν is the observing frequency and α is the scaling index (J. M. Cordes et al. 1985). For a Kolmogorov spectrum, $\alpha = 4.4$. However, some studies have found values of α smaller than 4.4 (e.g., N. D. R. Bhat et al. 2004; L. Levin et al. 2016; J. E. Turner et al. 2021). This may be caused by a non-Kolmogorov scattering screen or modulation by RISS (J. M. Cordes & B. J. Rickett 1998).

In this paper, we will focus on the effects of DISS on pulse arrival time. DISS leads to a distribution of path lengths from what was originally a plane wave, delaying the arrival of the emission and imparting a scattering tail upon the pulse profile (e.g., N. D. R. Bhat et al. 2004). Though J. E. Turner et al. (2021) found that PTA observatories at the time were not measuring time of arrival (TOA) variations with enough precision for DISS to cause significant delays, they stated that it will become a problem as instruments and timing analysis methods improve. Scattering also broadens the shape of the pulse, mostly affecting the trailing edge. The time variability of said pulse broadening throws off TOA measurements due to time-averaged pulse profile templates with fixed tail lengths (P. B. Demorest et al. 2013; G. Agazie et al. 2023a).

Collaborations such as NANOGrav that observe PTAs monitor changes in pulse arrival times over long periods of time—years or longer. Since scattering delays also vary over that timescale due to relative motions of the pulsar, Earth, and the ISM, (e.g., D. A. Hemberger & D. R. Stinebring 2008; L. Levin et al. 2016; J. E. Turner et al. 2021), it is important to monitor and correct for them as pulsar timing gets precise enough for scattering to be a significant source of noise.

PSR J0332+5434 (also known as PSR B0329+54) is the brightest pulsar visible to the Allen Telescope Array (ATA) and it has been the subject of pulsar scintillation research for decades (D. R. Stinebring et al. 1996). N. Wang et al. (2005) found that PSR J0332+5434 has a typical scintillation bandwidth of 5–15 MHz at 1540 MHz with a spectral index α of 3.3. The R.A. and decl. of this object are 03:32:59 and +54:34:43, respectively (A. T. Deller et al. 2019). It is relatively bright at ∼200 mJy (D. R. Lorimer et al. 1995), so it is visible even at higher frequencies.

This paper mainly focuses on the scintillation bandwidth and scaling index, but the literature for this pulsar is expansive and covers many other properties related to scintillation. B. J. Rickett (1970) began the search into PSR J0332+5434's scintillation bandwidth at 408 and 610 MHz. Many other studies followed, investigating the scintillation bandwidth, scintillation timescale, refractive timescale, and scaling index (e.g., A. Wolszczan et al. 1974, 1981; B. J. Rickett 1977; J. W. Armstrong & B. J. Rickett 1981; A. G. Lyne & F. G. Smith 1982; A. Wolszczan 1983; F. G. Smith & N. C. Wright 1985; J. M. Cordes 1986; Y. Gupta et al. 1994; V. M. Malofeev et al. 1996; D. R. Stinebring et al. 1996; N. D. R. Bhat et al. 1998, 1999; V. I. Kondratiev et al. 2001; N. Wang et al. 2005, 2008; W. Lewandowski et al. 2011; E. R. Safutdinov et al. 2017; P. F. Wang et al. 2018; Z. Wu et al. 2022; J. E. Turner et al. 2024b). The average scintillation bandwidth measured, scaled to 1426 MHz with Kolmogorov scaling ($\alpha = 4.4$), is ∼30 MHz, though there is a very wide spread. Even within individual studies, significant variation in bandwidth measurements were found (e.g., A. Wolszczan et al. 1974). The average scintillation timescale is ∼780 s, again scaled to 1426 MHz with Kolmogorov scaling ($\alpha = 1.2$), ranging from 6.8 s (V. I. Kondratiev et al. 2001) to 1797 s (N. D. R. Bhat et al. 1998). Measurements for the refractive timescale vary significantly as well, from 5 hr at 4.8 GHz (W. Lewandowski et al. 2011) to 206 days at 150 MHz (Z. Wu et al. 2022). Refractive timescales are discussed further in Section 4.3. The scaling index is discussed in Section 5.1.

In this paper, we present an in-depth study of PSR J0332+5434 and the variations in scintillation bandwidth over a 300 day period, aiming to characterize the scintillation behavior to explore how pulsar timing efforts might correct and remove similar delays in MSP data. Section 2 details the observations and data processing. Section 3 describes the method of making scintillation measurements, including generation and stretching of dynamic spectra and the use of two-dimensional autocorrelation functions (2DACFs). Section 4 provides an analysis of the time variability of scintillation bandwidths and compares the behavior of two subbands. Section 5 provides an investigation into the scaling index α and includes a novel method for its calculation. We conclude and discuss our results in Section 6.

2. Observations

2.1. The Allen Telescope Array

The ATA is a 42-dish radio interferometer located at the Hat Creek Radio Observatory (HCRO), California, and is owned

[11] The literature often uses α to represent this variable. Here, we will use x to disambiguate from the scaling index α.

Table 1
Observations of J0332+5434

Observing Campaign	Number of Observations	Total Time Observed (ks)	Start Date	End Date
Pilot	1	1.796	2022 Nov 8	2022 Dec 21
V1	232	131.6	2023 Feb 23	2023 Sep 1
V2	164	98.06	2023 Sep 7	2023 Dec 25

Note. Number and total observation time for each observing campaign. Each scan in the pilot campaign was around 30 minutes in length, while all subsequent scan lengths were around 10 minutes. There were 397 observations total, with total observing time 231.4 ks. The pilot observation was excluded from analysis due to the length of time between it and the first V1 observation.

and operated by the SETI Institute. Each element is an offset Gregorian 6.1 m in diameter containing a dual-polarization log-periodic "Antonio" feed that is instantaneously sensitive from 1 to 11 GHz. The feeds are cryogenically cooled to 70 K to maintain optimal sensitivity. Analog signals from the feeds are amplified and sent to the signal processing room over optical fiber; these signals are then split into four independently tunable signal chains ("a," "b," "c," and "d"), controlled by four independent local oscillators (LOs). Each tuning is capable of sampling 672 MHz of bandwidth anywhere in the radio frequency range of the ATA feed. Details of the ongoing upgrade program of the ATA will be described in forthcoming papers (W. Farah et al. 2025, in preparation; A. W. Pollak et al. 2025, in preparation).

Data from all tunings are then digitized and transmitted to the network on a 100 Gb ethernet link. In its current configuration, the digitization system can support 28 of the 42 antennas at two dual-polarization tunings, but at the time of this work, only 20 of the 42 antennas were available. With the ongoing refurbishment, the full array will be upgraded with new feeds and full four-tuning support by the end of 2026.

The ATA hosts a variety of digital signal processing (DSP) backends available for observers conducting different types of science investigations. For this project, we utilized the in-house built beamformer backend `BLADE` (L. F. Cruz et al. 2025, in preparation). `BLADE` has been fully tested and deployed on the ATA and allows the user to set science case dependent variables including the time and frequency resolution, the number of synthesized beams and their locations, and the desired polarization output product. The beamformer output can be set to SIGPROC filterbank[12] or filterbank HDF5, with each tuning outputting seven frequency-consecutive subband files, each covering 96 MHz bandwidth. Prior to each observing block, a GPU-based cross-correlation backend is used to target a flux calibrator, and instrumental delay, phase, and bandpass solutions are extracted and applied throughout the subsequent beamformer observations.

2.2. Observations

Observations of PSR J0332+5434 were done as part of an ATA observing campaign where ∼20 pulsars were monitored over the course of a year. This campaign went through three versions, as shown in Table 1. For all three versions, we chose a frequency resolution of 0.5 MHz, leading to 1344 frequency channels across each of the two 672 MHz tunings. The two tunings were centered at 1236 MHz (the lower tuning, "LOb") and 1908 MHz (the higher tuning, "LOc"), giving 1.344 GHz of total contiguous bandwidth from 900 to 2244 MHz; which is ideal for pulsar observing because it utilizes the ATA's wide bandwidth at the bottom of its sensitivity range, where the pulsars are brightest. We did not change the frequency tunings over the course of the project, however, we did see a significant impact from radio frequency interference (RFI) in this band. At first, we selected a sampling time of 64 μs, and chose a subintegration length of 10 s to accumulate sufficient pulsar signal. Soon after the start of V1 of the campaign, on 2023 March 7, the sampling time was changed from 64 μs to 16 μs to better resolve MSPs in the target set. While 64 μs is more than sufficient to resolve MSPs for scintillation purposes, we wanted to resolve multiple bins across the pulse for even the shortest-period pulsars in the set so that more resolution-dependent science may be done in future studies. Only Stokes-*I* intensities were saved, as polarization was not a focus of this work.

To track long-term variations in the scintillation bandwidth, observations of each pulsar are needed frequently (at least once a week) and over a long time-span (months to years). Observations of PSR J0332+5434 were done semiregularly three to four times a week at varying times of day in V1 of the survey, from 2023 February 23 to 2023 September 1, with each scan lasting approximately 10 minutes. During this time period, PSR J0332+5434 was sometimes observed several times in quick succession, including 32 10 minute scans over the entire 16 hr the source was above the horizon on 2023 August 19. Starting 2023 September 7 (for V2) the campaign was focused, with scans of PSR J0332+5434 and eight other pulsars done nearly every day, at approximately the same sidereal time. See Figure 1 for our observation timeline.

2.3. File Handling

Beamformed observations from each of the 96 MHz subbands are saved to disk in filterbank `SIGPROC` format (D. R. Lorimer 2011) and are processed with the standard `DSPSR` toolkit (W. van Straten & M. Bailes 2011) for dedispersion and pulsar folding at the DM (26.76 cm^{-3} pc; T. E. Hassall et al. 2012) and period (0.71 s; G. Hobbs et al. 2004, ephemeris generated at time of observation) of the pulsar, before writing the output in pulsar archive format (A. W. Hotan et al. 2004) with 1024 phase bins saved across the pulse. Data from all subbands are then moved to a permanent location, concatenated into a single pulsar archive per tuning, and later inspected for radio frequency interference.

In our observations, PSR J0332+5434 was very faint at the higher frequencies (above ∼2 GHz), which were also severely contaminated with RFI. It is for both these reasons that we used all seven LOb subbands, but only the four LOc subbands that were lowest in frequency, in the following analysis. For Sections 3 and 4, the first five LOb files (900–1380 MHz) were spliced together to make a file we refer to as "Band 1" in those

[12] https://sigproc.sourceforge.net/sigproc.pdf

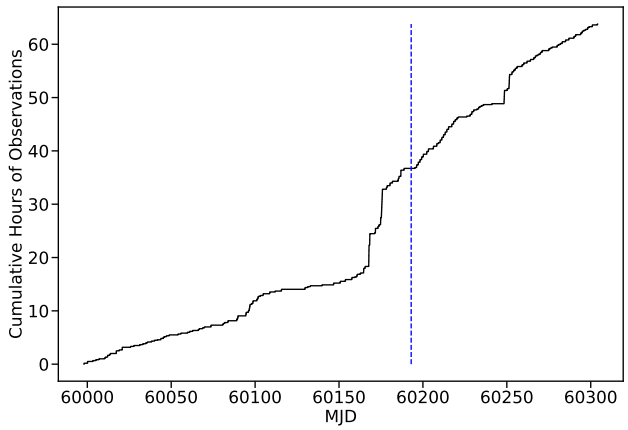

Figure 1. Cumulative observing time of PSR J0332+5434. Excluding the pilot observation, there were 396 observations resulting in 63.79 hr of total observation. The blue dashed line marks where Version 2 of the observing campaign began. Most observations were around 10 minutes in length. On average, we observed PSR J0332+5434 every 1.25 days, over 306 days.

sections, while the remaining two LOb and the four LOc files (1380–1956 MHz) were spliced together to make a file we refer to as "Band 2" in those sections. In Section 5, the bandpass was spliced into four files: 900–1092 MHz, 1092–1284 MHz, 1284–1572 MHz, and 1572–1956 MHz, respectively, labeled "Sub-Band 1," "Sub-Band 2," "Sub-Band 3," and "Sub-Band 4" in that section.

2.4. RFI Removal

Analysis began with RFI removal on the `.ar` files. Since observations were performed at *L*-band frequencies, the data showed significant RFI from GPS, as well as 3G and 4G mobile transmissions (CFR 2023). Manual RFI "zapping" was not possible for a data set of this size, so we used `clfd`, an automatic RFI zapper that uses a simple outlier detection method (V. Morello et al. 2018). Specifically, we used the standard deviation feature at the default threshold (two inter-quartile ranges used to determine the outliers to exclude from the distribution) to identify features that needed to be removed. This threshold was chosen to generally remove most of the RFI without affecting the brightest parts of the pulse. There were 23 Band 1 and 54 Band 2 measurements that were removed from the data sets due to RFI left over after zapping. There were also some dynamic spectra for which this method removed some of the frequency pixels at the brightest part of a scintle or scintles. This only noticeably occurred to ∼15% of the analyzed observations, and there was little to no effect on the final measurement made. On rare occasions, the algorithm zapped a large amount of frequency pixels right on the brightest part of a scintle, effectively cutting it in half and causing the measured scintillation bandwidth to be smaller than it should be. This was judged by eye, and only 11 Band 1 and 20 Band 2 measurements were removed from the data set due to this issue. A real-time RFI-mitigation algorithm is under development at the time of writing of this manuscript, an upgrade that will improve the quality of future data sets collected with the ATA beamformer.

3. Measuring the Scintillation Bandwidth

3.1. Dynamic Spectra

Dynamic spectra are plots of intensity over frequency and time; in this paper, each pixel in the dynamic spectrum represents the intensity of the pulse peak at that particular frequency and time. The majority of the observations were short (∼600 s) compared to the approximate 1 ks scintillation timescale of PSR J0332+5434 (D. R. Stinebring et al. 1996; V. I. Kondratiev et al. 2001; N. Wang et al. 2005, 2008; E. R. Safutdinov et al. 2017; P. F. Wang et al. 2018). Therefore, the scintles in our data appear as horizontal stripes in our dynamic spectra, leaving us unable to resolve the scintillation timescale.

Because the scintillation bandwidth is frequency-dependent according to Equation (4), we must correct for this effect by stretching the dynamic spectrum to normalize the scintle size for large bandpasses like those of the ATA. This allows for the whole bandpass to be analyzed simultaneously, which greatly improves the signal-to-noise ratio (S/N) of the 2DACF. The dynamic spectra for Band 1 and Band 2 were generated with `PyPulse` (M. T. Lam 2017) and stretched with reference to 1140 MHz and 1668 MHz (the center frequencies of the two bands), respectively; i.e., the size of the scintles across the spectrum are stretched or scrunched to be the same size as they would be at those reference frequencies. The right panel of Figure 2 shows an example of these "stretched" dynamic spectra. Note that stretching to an incorrect scaling index α could introduce some bias in the scintillation measurement. This is discussed in Section 5.

3.2. 2DACF

To extract the scintillation bandwidth from dynamic spectra, we employ a 2DACF. The autocorrelation function (ACF) correlates the dynamic spectrum to itself at different time and frequency lags, revealing the bandwidth and timescale at which the data stays self-similar. In Figure 3, we provide an example of some 2DACFs of PSR J0332+5434, again generated with `PyPulse`. Here, we are only interested in the variation along the frequency lag axis because we cannot resolve scintillation in time due to our short observations. Therefore, we then summed the 2DACF along the time axis to get a one-dimensional profile of the ACF along the frequency axis, as shown in Figure 4.

3.3. Fitting for the Scintillation Bandwidth

It has been shown that the appropriate analytical form for fitting a scintillation bandwidth from data such as that in Figure 4 is a Lorentzian (J. M. Cordes et al. 1985). Traditionally, Gaussian fits have been used to characterize ACFs in the literature, but the ISM impulse response function is assumed to be characterized by a one-sided exponential function, which is a Fourier pair with the Lorentzian function (J. E. Turner et al. 2024a). Thus, we use a Lorentzian here. The scintillation bandwidth is equivalent to the the HWHM of the Lorentzian.

Each ACF profile was first automatically fit with a single Lorentzian using the software package `SciPy` and function `optimize.curve_fit` (P. Virtanen et al. 2020) to correct for any large-bandwidth behavior that would cause errors in the returned properties of the central peak. This first fit was subtracted from the original profile and the resulting new profile was automatically fit with a narrower, single Lorentzian, as in K. R. Sand et al. (2022). This second Lorentzian fits to the central feature of the profile, and the HWHM is taken to be the scintillation bandwidth. This automatic stacked double-Lorentzian

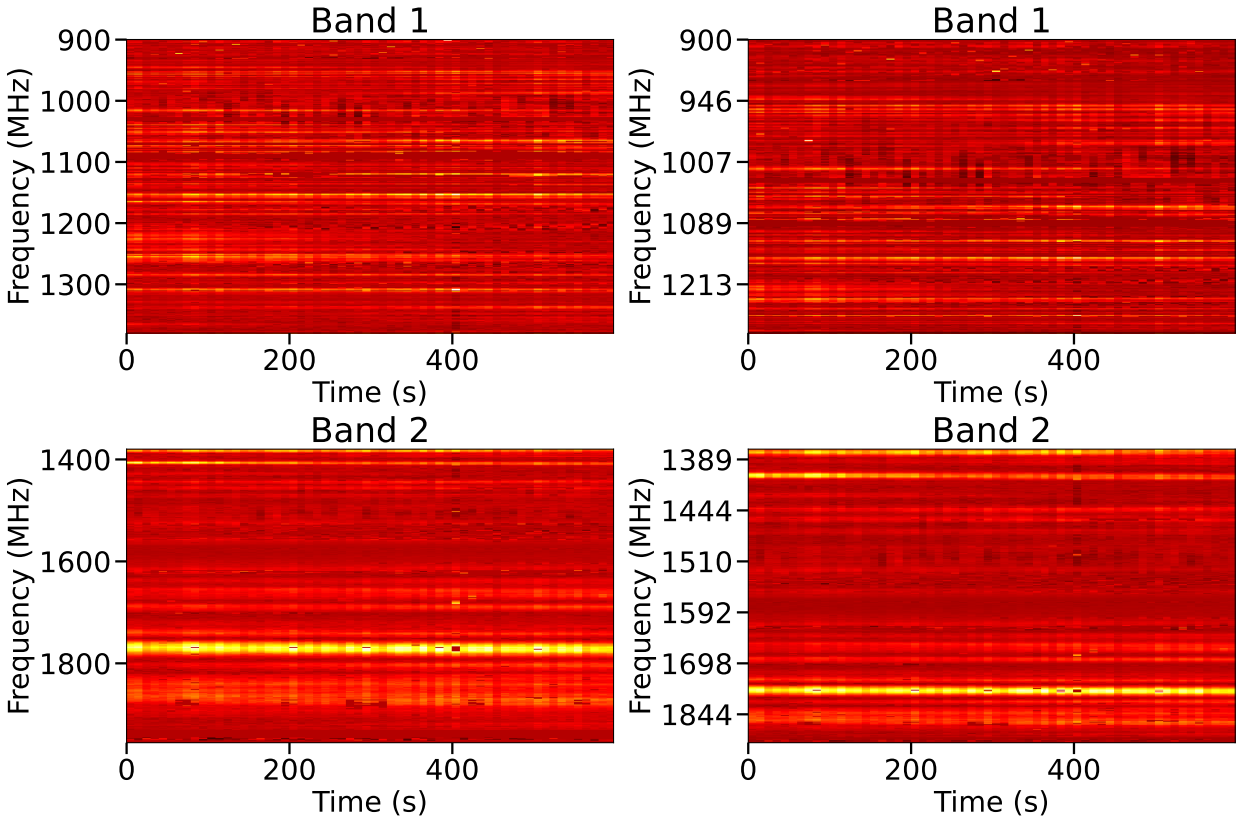

Figure 2. Example dynamic spectra for PSR J0332+5434 taken on MJD 60164, with time (in seconds) on the x-axis and frequency (in MHz) on the y-axis. The top plots show the lower frequencies (Band 1) while the bottom plots show the higher frequencies (Band 2). The plots on the left show the unmodified dynamic spectra, while the plots on the right show the same spectra "stretched" vertically to a Kolmogorov scaling index ($\alpha = 4.4$) to normalize scintle size over the wide bandwidth with reference frequencies 1139.75 MHz and 1667.75 MHz for Band 1 and Band 2, respectively.

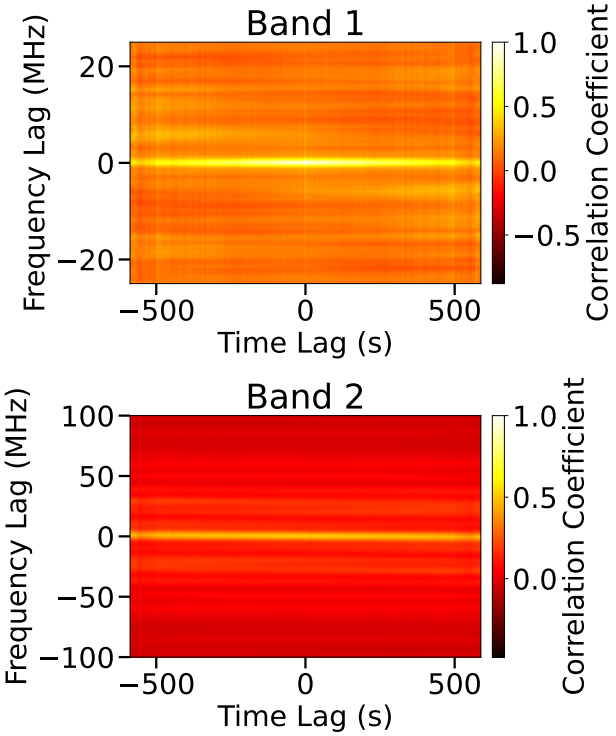

Figure 3. An example 2DACF from an observation of PSR J0332+5434 taken on MJD 60164, cropped to emphasize the central peak. The 2DACFs look horizontally banded due to our ability to resolve scintles in frequency, but not in time. The scintillation bandwidth $\Delta\nu_d$ is extracted from the width of the bright stripe at a frequency lag of 0.

fitting approach is robust to unusual profile shapes; this is necessary due to the size of the data set and reduces the chance of subjective human bias in the fitting process. Figure 4 shows an example of this double-Lorentzian fit.

Due to the frequency dependence of scintillation, it is possible for the scintillation bandwidth at low frequencies to be smaller than our receiver's resolution. Therefore, each Band 1 ACF was manually reviewed to ensure there were at least five points across the central structure of the ACF profile to fit a Lorentzian to, as in S. Sheikh et al. (2024).

3.4. Calculating Errors

The scintillation bandwidth measurement extracted in Section 3.3 is subject to three major sources of error: finite scintle error (FSE), the error on the Lorentzian fit from `scipy.optimize.curve_fit`, and the error due to the finite frequency resolution of the instrument.

FSE takes into account the fact that our bandwidth is not infinite, and that some scintles, especially larger ones, will be truncated at the edges of the bandpass. FSE can be described as:

$$\sigma_{\rm fse} = \frac{\Delta\nu_d}{2\log 2\sqrt{N_d}} \tag{5}$$

where

$$N_d = 1 + \frac{\eta\Delta\nu_{\rm receiver}}{\Delta\nu_d}, \tag{6}$$

(J. M. Cordes 1986) and η is the filling factor, set to 0.2 (as in J. M. Cordes & R. M. Shannon 2010; L. Levin et al. 2016;

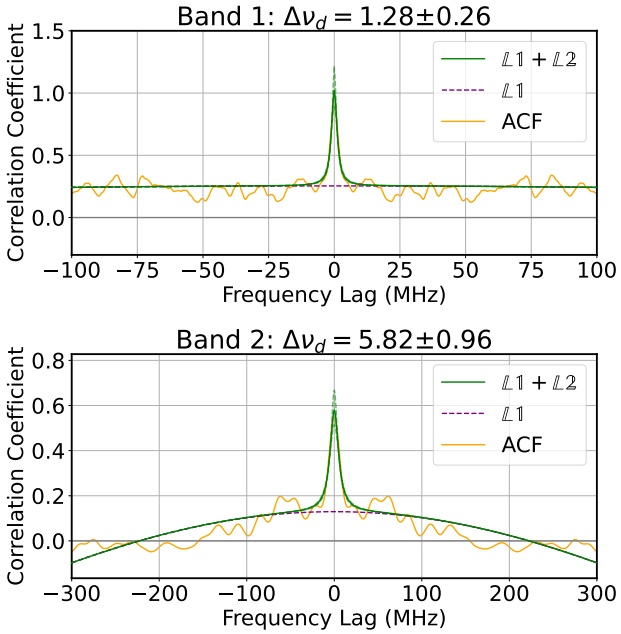

Figure 4. Example 2DACF profiles from an observation of PSR J0332+5434 taken on MJD 60164, summed across the time axis from Figure 3 (shown in orange), and cropped to emphasize the central peak. The 2DACF profiles have a clear peak with definite width around a frequency lag of zero and are well-described by the best-fit Lorentzian curves. The stacked double-Lorentzian fits, as described in Section 3.3, and their associated errors, are shown overlaid in green. The purple dotted line depicts the first Lorentzian ($\mathbb{L}1$) that was subtracted from the profile to ensure a correct fit to the central peak with the second Lorentzian ($\mathbb{L}2$). Band 1 and Band 2 are centered at 1139.75 MHz and 1667.75 MHz, respectively.

J. E. Turner et al. 2021). We then added in quadrature this FSE error, the error on the Lorentzian fit (the square root of the variance on the width), and the error due to the receiver's frequency resolution (0.25 MHz; this value is significant for smaller scintles, i.e., where FSE is small). The resulting 1σ error is shown on the output fit plots in Section 4.1.

3.5. Scattering Delay

Finally, for high-precision timing analysis, it is more useful to discuss the scattering delay τ_d rather than the scintillation bandwidth $\Delta\nu_d$, so we also list scattering delays for convenience. Using the measurement of the scintillation bandwidth from Section 3.3 and a propagation of errors from Section 3.4, we can find the scattering delay by rearranging Equation (1) for τ_d and setting $C_1 = 1$.

4. Time Series Analysis

4.1. Long-term Trends

PSR J0332+5434 was observed 397 times over 306 days. Some scans were removed at different steps of the analysis process due to, e.g., excessive RFI, corrupted or missing observational data, or low S/N. Pulsars are fainter at higher frequencies due to their steep spectral index; therefore, data from Band 2 consistently had lower S/N, resulting in the auto-fitter failing to return a successful fit more often on Band 2 than Band 1. Of the 397 observations, 342 measurements on Band 1 and 294 measurements on Band 2 were deemed reliable by manual review and were used in the following time series analysis.

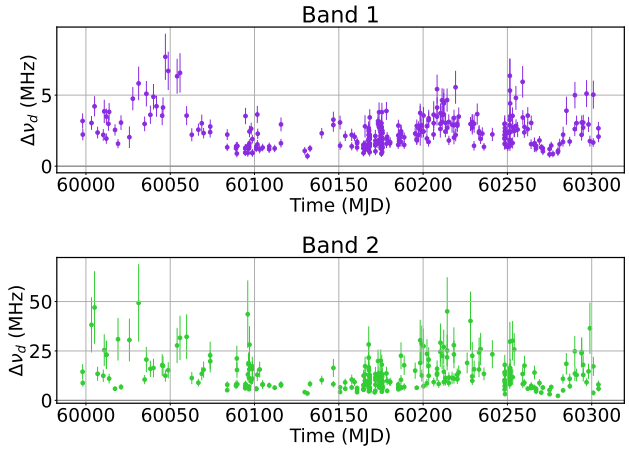

Figure 5. Measurements of scintillation bandwidth $\Delta\nu_d$ (y-axis) over a year of observation (x-axis) of J0332+5434. Band 1 (1140 MHz) is shown in purple (top panel), and Band 2 (1668 MHz) is shown in green (bottom panel). We show 1σ errors on the measurements via vertical error bars.

For the initial time series analysis, we stretched the dynamic spectra with Kolmogorov scaling, $\alpha = 4.4$, as is common in the literature. For Band 1, the minimum and maximum measurements were 0.71 ± 0.22 MHz and 7.70 ± 1.63 MHz, respectively, and the mean and standard deviation of the set of daily averages were 2.64 ± 1.26 MHz. The measurements from Band 2 ranged from a minimum of 2.27 ± 0.39 MHz to a maximum of 49.3 ± 19.6 MHz, with the mean and standard deviation of daily averages 14.7 ± 9.1 MHz. We also calculated the scattering delays using Equation (1). For Band 1, the minimum and maximum scattering delay measurements were 0.021 ± 0.004 μs and 0.23 ± 0.07 μs, respectively, and the mean and standard deviation of the set of daily averages were 0.06 ± 0.03 μs. The delays from Band 2 ranged from a minimum of 0.003 ± 0.001 μs to a maximum of 0.07 ± 0.01 μs with a mean and standard deviation of daily averages of 0.011 ± 0.006 μs. Daily averages were used to calculate the mean to account for irregularly spaced observations. Figures 5 and 6 show the time series in terms of scintillation bandwidth and scattering delay, respectively.

On average, our measurements were consistent with the predicted NE2001 scintillation bandwidths of $4.1^{+7.0}_{-1.8}$ and $22.1^{+37.6}_{-9.9}$ MHz for reference frequencies 1140 MHz and 1668 MHz, respectively. The errors on these NE2001 predictions assume a 20% distance error, but it should be noted that there are several other assumptions and errors to consider when predicting a value based on NE2001 (J. M. Cordes & T. J. W. Lazio 2002). Although our measurements of the mean for each band were consistent with the NE2001 predictions, there were 147 Band 1 measurements (43%) and 139 Band 2 measurements (47%) that were significantly less than the NE2001 predictions. No measurements were significantly larger than the NE2001 predictions. Since our measurements were consistently under the NE2001 predictions, this indicates that the model with the default assumptions is unreliable if used as a constant term for correcting scattering effects.

The long-term trends in Band 1—for example, being consistently overestimated by NE2001 from MJD 60050 to MJD 60200—seemed to be mirrored, as expected, by Band 2, though the trends in Band 2 were obscured due to its lower S/N. The Spearman correlation coefficient between Band 1 and Band 2 was 0.51 with a p-value of $\sim 10^{-9}$, suggesting a high probability of moderate positive correlation. Correlation

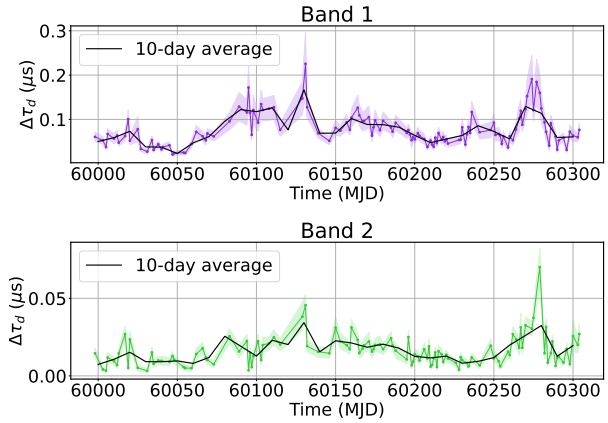

Figure 6. The daily average scattering delay $\Delta\tau_d$ (y-axis) over a year of observation (x-axis) of PSR J0332+5434. Band 1 is shown in purple (top panel), and Band 2 is shown in green (bottom panel). rms errors are shown via shading. The black line indicates the 10 day average, to emphasize longer timescale behavior. The long-term trends in Band 1—for example, having consistently higher delays from 60,050 to 60,200—seem to be mirrored, as expected, by Band 2, though the trends in Band 2 are obscured due to its lower S/N. The Spearman product-moment correlation coefficient is 0.51.

between bands is consistent with findings in D. A. Hemberger & D. R. Stinebring (2008).

4.2. Changes Over Time and Lomb–Scargle Periodicity

Figure 5 appears to show significant change in the scintillation bandwidth on the timescale of weeks to months. Splitting the data set into quarters (i.e., periods of ∼77 days) reveals significant change in the median over that time period. For Band 1, the median changed from 3.1 in the first 77 days to 1.4 MHz in the second. For Band 2, the medians of these same time periods changed from 16.4 to 8.2. This is a change of a factor of ∼2 in both bands during this time period.

While periodicity was not necessarily expected, there appeared to be some possible periodicity in the time series. Given a full time series of scintillation bandwidth, we investigated whether we saw any periodicity, which would make it possible to predict at least some aspects of scattering delay variability. To evaluate the presence of periodicity in unevenly sampled data, we used a Lomb–Scargle periodogram (J. D. Scargle 1982). Figure 7 shows the results of a Lomb–Scargle periodogram generated with `astropy.timeseries.LombScargle` (Astropy Collaboration et al. 2013) and subsequent sinusoidal models fit to the time series data. Initially, we did not include the bandwidth errors in the calculation of the period; larger measurements had larger errors, so we did this to avoid weighting the smaller measurements more than the larger measurements. The residuals from the sinusoid model had an rms of 1.00 and 7.50 MHz for Band 1 and Band 2, respectively. These were lower than the residual rms of a straight line with the same offset as the sinusoid midlines: 1.13 and 8.03 MHz, respectively.

The periodicity with the highest power was ∼204 days for both Band 1 and Band 2. However, the resolution for detecting this periodicity was very low given the ∼300 days observation period; it should be noted that $1/180$ and $1/204$ were adjacent points in the period-axis of the periodograms, for example. Given the low resolution in the period-axis, we could not prove definitively whether there was periodicity or what that period would be—χ^2 analysis returned a reduced χ^2 of 4.6 and 17.4, respectively, which indicated that the data did not match the model. However, our comparison of the median values at the beginning of this section corroborates the periodicity found by the Lomb–Scargle periodogram; the time periods with the greatest difference in median were adjacent periods of ∼77 days, which is roughly half the period found above. We tested that the results were robust to error through both a Monte Carlo (MC) analysis and by inputting the errors on each measurement directly into the `LombScargle` periodogram function. We found no notable change in results when incorporating the errors in this way.

4.3. Interpretations of Long-timescale Behavior

The results of Section 4.2 suggest some kind of long-term, potentially periodic, behavior in the time series of scintillation bandwidth measurements. Here we consider two explanations for this behavior: annual variations in line of sight from Earth's orbit and variations due to RISS.

To investigate potential annual variations in scintillation bandwidth, we fit an additional sinusoid to the data at a year-long period and compared it to the results of the Lomb–Scargle analysis. The 200 day period has smaller residual rms than a year-long period—it should be noted, however, that our observation period was less than a year, so this test is inconclusive as to whether a year-long period is consistent.

Y. Liu et al. (2022) finds annual variation in scintillation timescale in other pulsars, but not scintillation bandwidth. This is due to the timescale's dependency on the scintillation velocity $V_{\rm ISS}$, which includes the velocity due to Earth's orbit around the Sun. The scintillation bandwidth, on the other hand, only depends on the spatial scale of the diffractive scintillation pattern l_d and the observing frequency. Annual variations in $\Delta\nu_d$ can only be seen if the scattering screen is close to Earth or if l_d is small, due to how the line of sight moves through the screen in these scenarios. M. L. Putney & D. R. Stinebring (2006) and N. Wang et al. (2008) conclude that the scattering occurs closer to PSR J0332+5434 than to Earth, which casts additional doubt on the theory that the observed variation is caused by Earth's orbit around the Sun.

Another potential explanation for the variability we see is RISS. RISS occurs on longer timescales (typically weeks to years) and modulates the DISS measurements as potentially seen in Figure 5. The refractive timescale can be estimated by

$$T_r \approx \frac{4}{\pi}\left(\frac{\nu\Delta t_{\rm d}}{\Delta\nu_{\rm d}}\right), \tag{7}$$

which for $\nu \approx 1500$ MHz, $\Delta\nu_{\rm d} \approx 10$ MHz, and NE2001-derived scintillation timescale $\Delta t_{\rm d} \approx 675$ s is of order one day (D. R. Stinebring & J. J. Condon 1990). This is far less than the ∼200 day timescale we see in Figures 5 and 6.

However, in the calculation of Equation (7), we make implicit assumptions via the use of NE2001, e.g., about the velocity of the system (assuming a uniform $V_{\rm ISS} = 100\,{\rm km\,s^{-1}}$). This value should thus be taken as a rough estimate.

We can also compare to empirical measurements. J. E. Turner et al. (2024b) and N. Wang et al. (2005) found RISS timescales of ∼3 days. However, N. Wang et al. (2008) found a timescale of ∼8 hr, which is relatively consistent with the T_r estimate above. The ∼once a day observing cadence of our survey would not resolve variations on hour to day timescales. This indicates

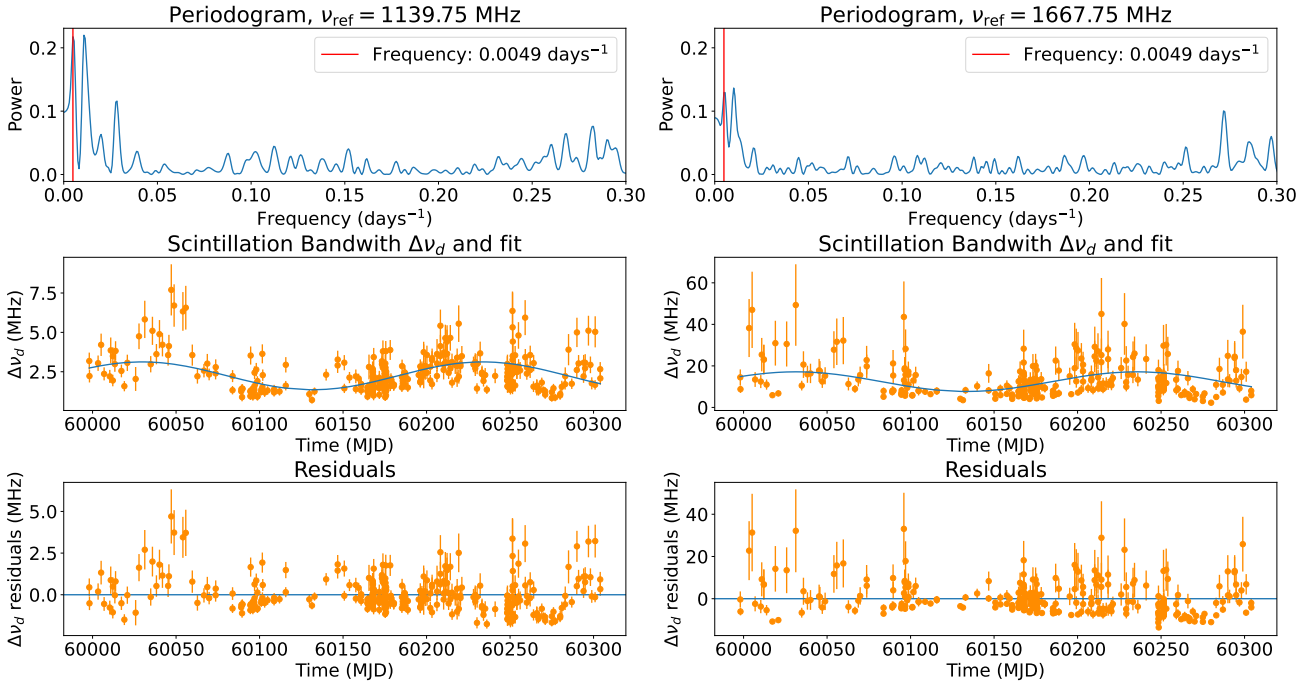

Figure 7. Lomb–Scargle model for the scintillation bandwidth, showing a periodicity of ∼204 days for both Band 1 (left panels) and Band 2 (right panels). Top panels show the Lomb–Scargle periodogram, middle panels show the sinusoid model fit to the data, and the bottom panels show the residuals of the sinusoid model fit. Due to this period approaching the length of our observing period, these fits are inconclusive.

that the long-timescale variations seen in our data may not be attributed to RISS.

In conclusion, neither RISS nor annual variations are particularly compelling explanations for the long-timescale behavior that we observe in Figure 5. A simultaneous combination of these effects could be responsible, but it is difficult to attribute a cause without a longer observing campaign that could better constrain periodicity.

4.4. Bandwidth Distribution

The data in Figure 5 seems to follow a slightly skewed distribution. To better characterize the distribution of scintillation bandwidths, we fit a log-normal distribution to the probability distribution function (PDF) and cumulative distribution function (CDF) of each set of data. To evaluate whether our results are consistent with a log-normal distribution with the form

$$f(x, s) = \frac{1}{sx\sqrt{2\pi}} \exp\left(-\frac{\log^2(x)}{2s^2}\right), \quad (8)$$

we estimated the distribution of measurements with an unweighted kernel-density estimate. We assumed a Gaussian kernel and then used the SciPy function `stats.gaussian_kde` using a bandwidth 0.38 computed by the default method "Scott's Rule" (D. W. Scott 2015). Figure 8 shows the PDF and CDF of the unscaled daily average bandwidth measurements compared with a log-normal distribution, the parameters of which were determined using the SciPy function `optimize.curve_fit` to be $s = 0.48$ and $\mu = 2.5$ for Band 1 and $s = 0.65$ and $\mu = 13.4$ for Band 2. We then ran an Anderson–Darling test on the CDFs of the data and the log-normal distribution, which returned p-values of 0.23 for Band 1 and 0.18 for Band 2, which are both higher than the significance threshold of 0.05. The peak of the best-fit log-normal distribution occurred at 2.00 MHz for Band 1 and 8.79 MHz for Band 2.

5. Scaling Index

5.1. Literature

As described in Section 3.1, the scintillation bandwidth is expected to increase as frequency increases according to Equation (4), where $\alpha = 4.4$ in a Kolmogorov medium. However, this scaling index is often found to be much shallower (e.g., D. A. Hemberger & D. R. Stinebring 2008; L. Levin et al. 2016; J. E. Turner et al. 2021).

L. Levin et al. (2016) used four 200 MHz unstretched subbands at a center frequency of 1500 MHz, found $\Delta\nu_d$ and τ_d using the ACF method described in Section 3.2, and performed a weighted linear fit in semilog space of τ_d to measure the scaling index. They found that α was shallower than 4.4 for most of the 10 pulsars observed and varied over a wide range ($2 < \alpha < 6$) for just one pulsar (PSR J1614–2230).

J. E. Turner et al. (2021) used this same subband method and found similar results, with additional evidence for time dependence of the scaling index. They also examined the scaling index across a wider frequency range, using both the 820 MHz band and 1500 MHz band and using the weighted average of scattering delays for those bands. Time-dependence could not be investigated with this method.

PSR J0332+5434 specifically has a few measurements of the scaling index in the literature. Z. Wu et al. (2022) measured the scaling index to be $\alpha = 4.46 \pm 0.06$, which agrees with Kolmogorov scaling ($\alpha = 4.4$). A. Wolszczan (1983) measured an index of 3.8 ± 0.1, which is significantly lower. However, fitting unscaled scintillation bandwidth measurements from the literature to an equation with the form of Equation (4) returns a scaling index of 3.8 ± 0.7, which agrees with A. Wolszczan (1983). See Figure 9.

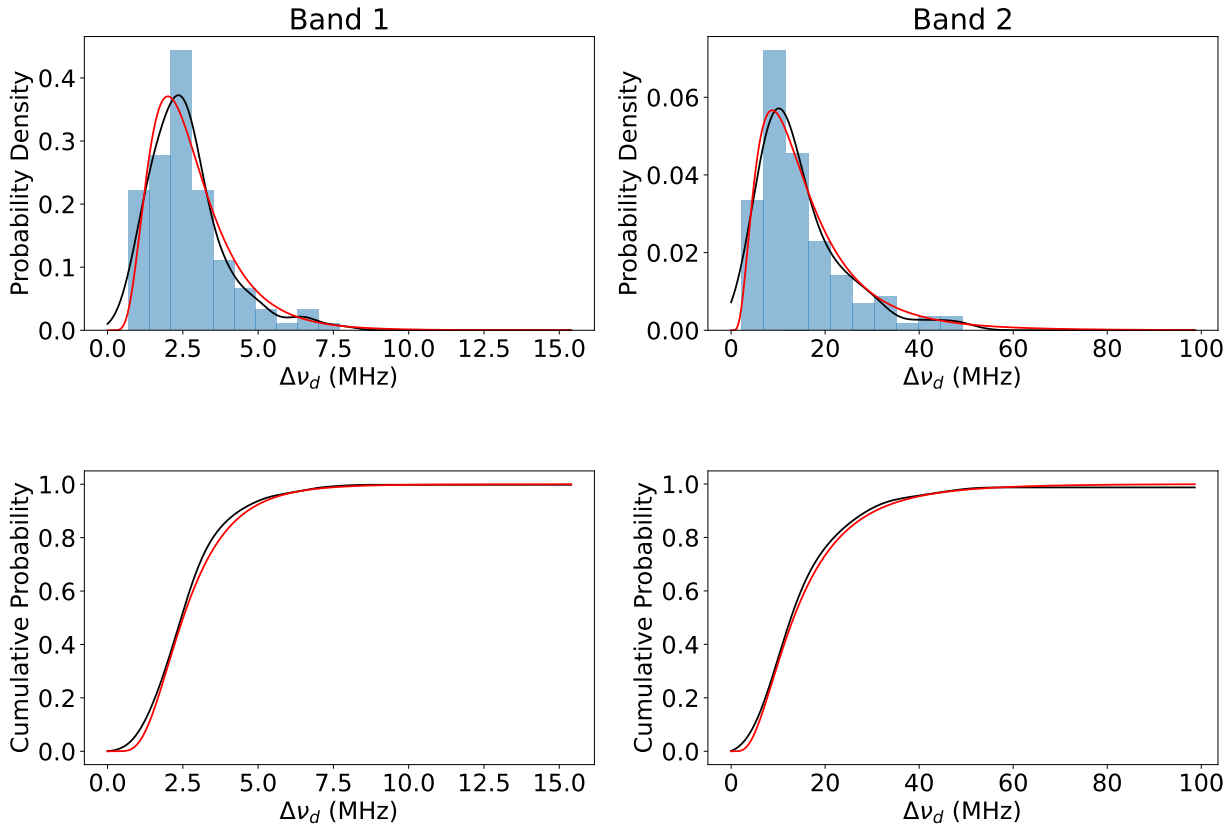

Figure 8. The unscaled daily average bandwidths (black) compared to a log-normal distribution (red).

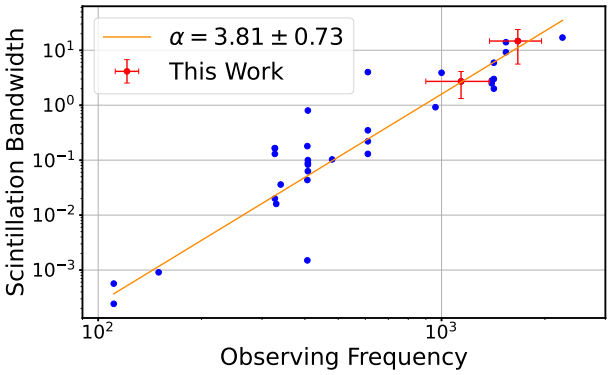

Figure 9. A comparison of measured scintillation bandwidth values from the literature for PSR J0332+5434. Measurements from Section 4.1 are included in red. The scaling index measured from these data points is shown as the orange line.

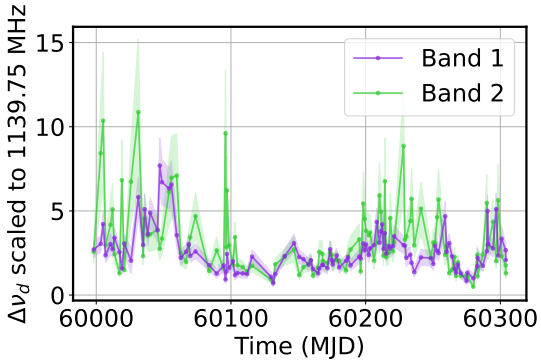

Figure 10. Daily averages of Band 1 (purple) and Band 2 (green) measurements of scintillation bandwidth $\Delta\nu_d$. Band 2 has been scaled to Band 1's reference frequency with a scaling index of $\alpha = 4.25$.

5.2. Two-band Methods

For our analysis of the scaling index, we performed three investigations. The first used the data already acquired in Section 4, where the bandwidth was divided into two bands. We scaled the Band 2 daily average time series to Band 1 using the relation in Equation (4), as seen in Figure 10. Using χ^2 analysis where Band 1 is the expected "model" scaled to fit the Band 2 data, we found the best-fit scaling index of the two bands to be 4.25, with a reduced χ^2 of 0.98.

We also used `optimize.curve_fit` to fit a curve of the form $\Delta\nu_d \propto \nu^\alpha$ to every measurement, as seen in Figure 11. We found a scaling index of ∼3.6.

5.3. Traditional Subband Method

We also examined the scaling index using similar methods to L. Levin et al. (2016) and J. E. Turner et al. (2021). The 900–1956 MHz bandpass was split into four subbands as described in Section 2.3. Scintillation bandwidth measurements were made using the method in Section 3 but leaving the dynamic spectra unstretched, which is possible due to the smaller size of the subbands. Each epoch was fit to a one-parameter function of the form $\Delta\nu_d \propto \nu^\alpha$. An example is shown in Figure 12.

Only observations that resulted in three or more bands with reliable measurements were used. Those with two or fewer measurements were excluded from analysis. Ultimately, 273 observations were included in analysis. We found α to range from 1.0 ± 0.5 to 7.2 ± 1.3, with a mean of 3.5 ± 1.1. The time series can be seen in Figure 13.

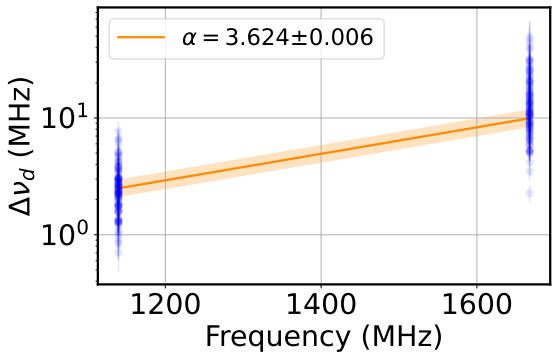

Figure 11. Daily average time series, Band 1 (1139 MHz) and Band 2 (1668 MHz), with the scaling index fit in semilog space. The scaling index was measured to be 3.624 ± 0.006.

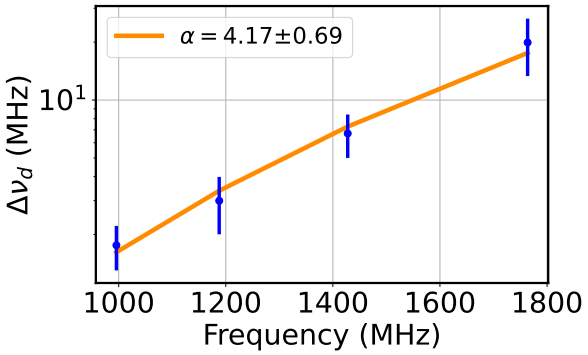

Figure 12. Example fit of the scaling index of a single observation on MJD 60010, in semilog space.

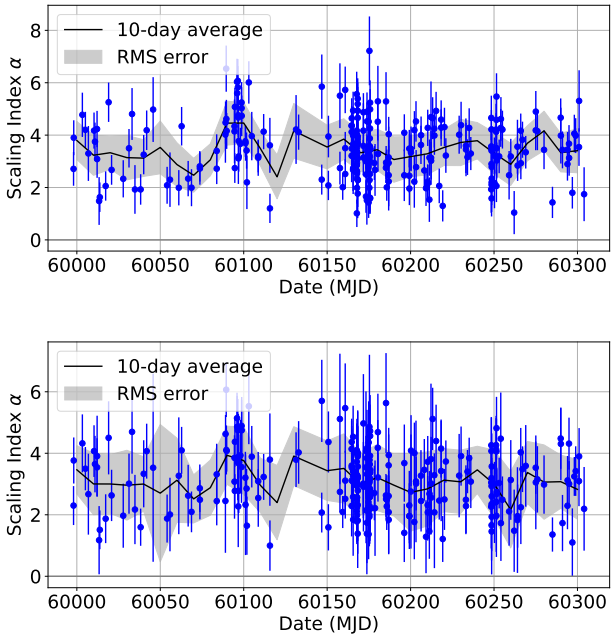

Figure 13. Time series of scaling index measurements over time using the established subband method (top panel) and the novel cross-subband method (bottom panel). The black line indicates the 10 day average with the rms error represented in the gray shaded area.

5.4. Cross-subband Method

The use of a constant spectral index when stretching the dynamic spectra potentially introduced some small error in the analysis in Sections 5.2 and 5.3. J. E. Turner et al. (2021) noted that stretching a dynamic spectrum by the wrong index

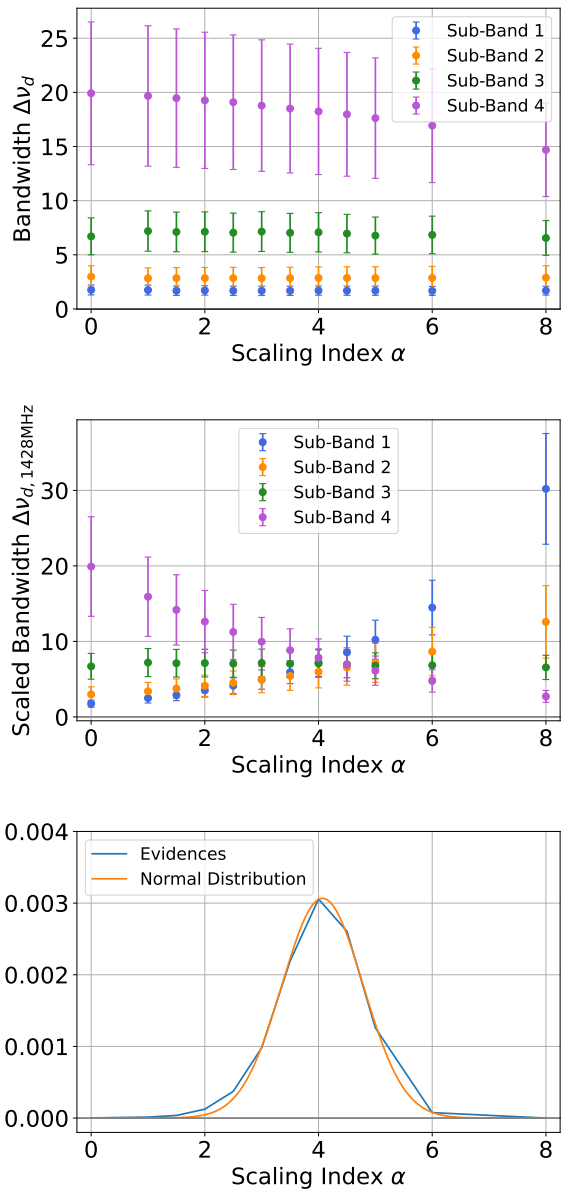

Figure 14. An example scaling index measurement of one observation taken on MJD 60010 made with the novel cross-subband method described in Section 5.4.

(between 1 and 5) can result in 10% fractional error. To remedy this, we present a third, newly developed method, here called the "cross-subband" method. We again split the bandwidth into four subbands. However, each dynamic spectrum was generated 12 times, each with a different scaling factor ranging from 0 to 8. Then, $\Delta\nu_d$ was measured for each dynamic spectrum using the method described in Section 3. The measurements were then scaled to reference frequency 1428 MHz using each spectrum's respective scaling index. These scaled measurements were then compared with each other using an evidence expression and conditional probabilities (see the Appendix) which was then fit with a normal distribution where the peak is at the measurement of the estimated scaling index and the width of the distribution is the error on the measurement. This process is shown in Figure 14.

As in Section 5.3, we only used observations that had measurements for three or more bands. We used the same 273 observations for this analysis. We found α to vary from 1.0 ± 0.8

to 6.1 ± 0.9 with a mean of 3.1 ± 1.0. The time series can be seen in Figure 13.

Our measurements are largely consistent with the established method (Section 5.3). Of the 273 observations, only 10 resulted in inconsistent measurements of the scaling index. The Pearson correlation coefficient between the two data sets was 0.80. While the established method returns measurements with lower errors, with an average error of 0.8 MHz as opposed to the novel method's average error of 1.0 MHz, those estimates rely on the fixed initial assumption of α when initially stretching the spectra. This is incongruent with the final measurements for α from this method, which span nearly an order of magnitude from 1 to 7 (see Section 5.3). In our new method, we relax this assumption, jointly inferring the initial α rather than imposing a prior, often incorrect, initial value. Our error is therefore larger, but more robust, as it incorporates the measurement noise and the previously unaccounted for uncertainty in the initial alpha stretching.

6. Discussion and Conclusions

Over about 300 days, we have monitored PSR J0332+5434 and made nearly daily measurements of its scintillation bandwidth over a large bandpass (900–1956 MHz). While long-term studies of pulsar scintillation over this time period or with this frequency of observation have been done before (e.g., D. A. Hemberger & D. R. Stinebring 2008; L. Levin et al. 2016; J. E. Turner et al. 2021), this study has done both with a larger bandpass.

First, we broke the bandpass into two bands and corrected for ISM scaling by assuming a Kolmogorov medium with $\alpha = 4.4$. We found the mean scintillation bandwidth $\Delta\nu_d$ to be 2.64 ± 1.26 MHz for Band 1 (1140 MHz) and 14.7 ± 9.1 MHz for Band 2 (1668 MHz). The scintillation bandwidth also varied significantly over time, with the median changing by a factor of 2.2 in Band 1 and 2.0 in Band 2 between two ∼77 day periods. Lomb–Scargle analysis indicates potential periodicity at ∼200 days, though our observing period was not long enough to confirm this claim.

Almost half of our scintillation measurements were significantly lower than the NE2001 predictions, indicating that NE2001 consistently overestimates the bandwidth when using the default assumptions. At most, NE2001 overestimated our measured values by a factor of 5 in Band 1 and a factor of 9 in Band 2.

Our bandwidth measurements were also shown to have a log-normal distribution, which shows the space of expected scintillation bandwidth measurements. The shape of the distribution of scintillation bandwidth measurements has not been commented on significantly in the literature.

In addition to assuming a Kolmogorov medium and scaling the dynamic spectra as such ($\alpha = 4.4$), we also investigated the scaling index with multiple methods. The best-fit scaling index for the two bands described above was found to be ∼3.6. We also divided the bandpass into four bands as described in Section 2.3. Using established multiband methods (such as those used by L. Levin et al. 2016 and J. E. Turner et al. 2021), we found an average spectral index of 3.5 ± 1.1. However, in order to make these measurements, the dynamic spectra were not stretched, potentially introducing some error. To correct for this, we developed a novel "cross-subband" method where dynamic spectra were generated multiple times per subband, each time stretched by a different index. Using this method (described in Section 5.4), we found an average scaling index of $\alpha = 3.1 \pm 1.0$. Comparing each measurement made with the new method to its corresponding measurement made with the established multiband method revealed that the two methods are quite consistent with each other. Though the new method generally resulted in larger error bars on the measurements, we believe these errors to be more robust than previous methods (see Section 5.4).

Due to having only one observable variable, there is little we can say on the structure of the ISM aside from a rough estimate of the scaling index. We are unable to make conclusions about the value of C_1 in Equation (1) or where along the line of sight potential scattering might occur. However, past studies of PSR J0332+5434 have proposed an extended scattering medium that is concentrated toward the pulsar (e.g., M. L. Putney & D. R. Stinebring 2006; N. Wang et al. 2008).

The data we have collected during this campaign appears to be a snapshot of the long-term scattering variability seen in pulsars. D. A. Hemberger & D. R. Stinebring (2008) observed PSR B1737+13 over a similar timescale to ours where they observed small variations on the timescale of about a week, similar to the peaks and valleys we see in Figure 6. They also saw a large change in the time series structure after ∼175 days of observation. W. A. Coles et al. (2015) observed two extreme scattering events (R. L. Fiedler et al. 1987) over their years-long observing campaign with the Parkes Pulsar Timing Array. These events are characterized by a large and sudden change in DM and flux, corresponding to a decrease in scintillation bandwidth. We have not observed any of these extreme events over our ∼300 day observing period—one that is relatively short compared to those of PTA projects (G. Agazie et al. 2023b).

Overall we have determined that the scintillation bandwidth, and therefore the scattering delay, varies too much to be predicted by a static value. We found the delay to vary by up to 70 ns. We were not able to confirm periodicity, but future work may be able to improve predictions of delay with time by executing campaigns with observing periods greater than a year. Future studies should continue to explore the effects observed here, and we encourage NANOGrav and other collaborations that observe PTAs to take this scintillation variation into account when making their measurements, as this work illustrates effects that might be seen for MSPs. PSR J0332+5434 is only one of nine pulsars observed during this campaign; while the other pulsars are fainter and therefore require better or more manual RFI and noise mitigation, the methods described here can be expanded to that data as well as MSPs in other data sets. Bright, slow pulsars like PSR J0332+5434 are not useful for high-precision timing themselves, but can help determine scattering contributions to the error budget for MSPs at different distances and in different directions of the sky.

Acknowledgments

The Allen Telescope Array refurbishment program and its ongoing operations are being substantially funded through the Franklin Antonio Bequest. Additional contributions from Frank Levinson, Greg Papadopoulos, the Breakthrough Listen Initiative, and other private donors have been instrumental in the renewal of the ATA. Breakthrough Listen is managed by the Breakthrough Initiatives, sponsored by the Breakthrough Prize Foundation. The Paul G. Allen Family Foundation provided major support for the design and construction of the ATA, alongside contributions from Nathan Myhrvold, Xilinx Corporation, Sun Microsystems, and other private donors. The ATA has also been supported by contributions from the US Naval Observatory and the US National Science Foundation. S. Z.S. acknowledges that this material is based upon work

supported by the National Science Foundation MPS-Ascend Postdoctoral Research Fellowship under grant No. 2138147. We acknowledge support received from NSF AAG award number 2009468 and NSF Physics Frontiers Center award number 2020265, which supports the NANOGrav project. The Pulsar Search Collaboratory is supported by NSF award No. 2425047. We acknowledge 2023 SETI Institute REU student Ella Hort for her RFI characterization work in *L* band at the ATA, enabled by the SETI Institute REU program, NSF award No. 2051007. Finally, we would like to acknowledge Foothill College student Brianna Bermudez for her contributions to this work.

Appendix
Evidences Expression

The following describes in detail the analysis method used in Section 5.4 to estimate the scaling index α. The measured scintillation bandwidths for a particular scintillation bandwidth are used to create a hypothetical normal distribution, with the bandwidth measurement acting as the mean μ and the error acting as the width σ. The evidence for a given scaling index is calculated by integrating the product of the likelihoods of each individual measured scintillation bandwidth

$$\int_{-\infty}^{\infty} \prod_{i=1}^{n} \mathcal{N}(x|\mu_i,\, \sigma_i^2)\, dx, \tag{A1}$$

where $\mathcal{N}$ represents the probability density function for each measured scintillation bandwidth. For observations with three bands, the simplified evidence expression is

$$\frac{\sqrt{\sigma_1^2+\sigma_2^2}\exp\left[\dfrac{-\mu_1^2\sigma_2^2\sigma_3^2-\mu_2^2\sigma_1^2\sigma_3^2-\mu_3^2\sigma_1^2\sigma_2^2+\frac{(\mu_3\sigma_1^2\sigma_2^2+\sigma_3^2(\mu_1\sigma_2^2+\mu_2\sigma_1^2))^2}{\sigma_1^2\sigma_2^2+\sigma_1^2\sigma_3^2+\sigma_2^2\sigma_3^2}}{2\sigma_1^2\sigma_2^2\sigma_3^2}\right]}{2\pi\sqrt{\sigma_1^4\sigma_2^2+\sigma_1^4\sigma_3^2+\sigma_1^2\sigma_2^4+2\sigma_1^2\sigma_2^2\sigma_3^2+\sigma_2^4\sigma_3^2}} \tag{A2}$$

and for four bands

$$\frac{\sqrt{2}\exp\left[-\dfrac{\mu_1^2}{2\sigma_1^2}-\dfrac{\mu_2^2}{2\sigma_2^2}-\dfrac{\mu_3^2}{2\sigma_3^2}-\dfrac{\mu_4^2}{2\sigma_4^2}+\dfrac{(\mu_1\sigma_2^2\sigma_3^2\sigma_4^2+\mu_2\sigma_1^2\sigma_3^2\sigma_4^2+\mu_3\sigma_1^2\sigma_2^2\sigma_4^2+\mu_4\sigma_1^2\sigma_2^2\sigma_3^2)^2}{2(\sigma_1^4\sigma_2^4\sigma_3^4\sigma_4^2+\sigma_1^4\sigma_2^4\sigma_3^2\sigma_4^4+\sigma_1^4\sigma_2^2\sigma_3^4\sigma_4^4+\sigma_1^2\sigma_2^4\sigma_3^4\sigma_4^4)}\right]}{4\pi^{\frac{3}{2}}\sqrt{\sigma_1^2\sigma_2^2\sigma_3^2+\sigma_1^2\sigma_2^2\sigma_4^2+\sigma_1^2\sigma_3^2\sigma_4^2+\sigma_2^2\sigma_3^2\sigma_4^2}}. \tag{A3}$$

The expression is computed for each scaling index and the results are plotted. These results are then fit with a normal distribution using `scipy.optimize.curve_fit`. The mean μ of this fit is taken to be the estimated scaling index and σ is taken as the error on the estimation.

ORCID iDs

Grayce C. Brown https://orcid.org/0000-0002-0069-2778
Sofia Z. Sheikh https://orcid.org/0000-0001-7057-4999
Luigi F. Cruz https://orcid.org/0000-0001-5576-2254
Wael Farah https://orcid.org/0000-0002-0161-7243
Vishal Gajjar https://orcid.org/0000-0002-8604-106X
Christian Gilbertson https://orcid.org/0000-0002-1743-3684
Michael T. Lam https://orcid.org/0000-0003-0721-651X
Maura McLaughlin https://orcid.org/0000-0001-7697-7422
Alexander W. Pollak https://orcid.org/0000-0002-3430-7671
Andrew Siemion https://orcid.org/0000-0003-2828-7720
Gurmehar Singh https://orcid.org/0000-0001-7198-9459

References

Agazie, G., Alam, M. F., Anumarlapudi, A., et al. 2023a, ApJL, 951, L9
Agazie, G., Anumarlapudi, A., Archibald, A. M., et al. 2023b, ApJL, 951, L8
Alam, M. F., Arzoumanian, Z., Baker, P. T., et al. 2021, ApJS, 252, 4
Armstrong, J. W., & Rickett, B. J. 1981, MNRAS, 194, 623
Astropy Collaboration, Robitaille, T. P., Tollerud, E. J., et al. 2013, A&A, 558, A33
Bhat, N. D. R., Cordes, J. M., Camilo, F., Nice, D. J., & Lorimer, D. R. 2004, ApJ, 605, 759
Bhat, N. D. R., Gupta, Y., & Rao, A. P. 1998, ApJ, 500, 262
Bhat, N. D. R., Rao, A. P., & Gupta, Y. 1999, ApJS, 121, 483
CFR 2023, Table of Frequency Allocations and Radio Regulations 2023, FCC https://www.federalregister.gov/documents/2023/06/07/2023-11972/table-of-frequency-allocations-and-radio-regulations
Coles, W. A., Kerr, M., Shannon, R. M., et al. 2015, ApJ, 808, 113
Cordes, J. M. 1986, ApJ, 311, 183
Cordes, J. M., & Lazio, T. J. W. 2002, arXiv:astro-ph/0207156
Cordes, J. M., & Rickett, B. J. 1998, ApJ, 507, 846
Cordes, J. M., & Shannon, R. M. 2010, arXiv:1010.3785
Cordes, J. M., Weisberg, J. M., & Boriakoff, V. 1985, ApJ, 288, 221
Deller, A. T., Goss, W. M., Brisken, W. F., et al. 2019, ApJ, 875, 100
Demorest, P. B., Ferdman, R. D., Gonzalez, M. E., et al. 2013, ApJ, 762, 94
Fiedler, R. L., Dennison, B., Johnston, K. J., & Hewish, A. 1987, Natur, 326, 675
Gupta, Y., Rickett, B. J., & Lyne, A. G. 1994, MNRAS, 269, 1035
Hassall, T. E., Stappers, B. W., Hessels, J. W. T., et al. 2012, A&A, 543, A66
Hemberger, D. A., & Stinebring, D. R. 2008, ApJL, 674, L37
Hobbs, G., Lyne, A. G., Kramer, M., Martin, C. E., & Jordan, C. 2004, MNRAS, 353, 1311
Hotan, A. W., van Straten, W., & Manchester, R. N. 2004, PASA, 21, 302
Kolmogorov, A. 1941, DoSSR, 30, 301
Kondratiev, V. I., Popov, M. V., Soglasnov, V. A., & Kostyuk, S. V. 2001, Ap&SS, 278, 43
Lam, M. T., 2017 PyPulse: PSRFITS Handler, Astrophysics Source Code Library, ascl:1706.011
Levin, L., McLaughlin, M. A., Jones, G., et al. 2016, ApJ, 818, 166
Lewandowski, W., Kijak, J., Gupta, Y., & Krzeszowski, K. 2011, A&A, 534, A66
Liu, Y., Main, R. A., Verbiest, J. P. W., et al. 2023, SCPMA, 66, 119512
Liu, Y., Verbiest, J. P. W., Main, R. A., et al. 2022, A&A, 664, A116
Lorimer, D. R., 2011 SIGPROC: Pulsar Signal Processing Programs, Astrophysics Source Code Library, ascl:1107.016
Lorimer, D. R., Yates, J. A., Lyne, A. G., & Gould, D. M. 1995, MNRAS, 273, 411
Lyne, A. G., & Smith, F. G. 1982, Natur, 298, 825
Malofeev, V. M., Shishov, V. I., Sieber, W., et al. 1996, A&A, 308, 180
Morello, V., Barr, E. D., Cooper, S., et al. 2018, MNRAS, 483, 3673
Narayan, R. 1992, RSPTA, 341, 151
Putney, M. L., & Stinebring, D. R. 2006, ChJAS, 6, 233
Rickett, B. J. 1970, MNRAS, 150, 67
Rickett, B. J. 1977, ARA&A, 15, 479
Safutdinov, E. R., Popov, M. V., Gupta, Y., Mitra, D., & Kumar, U. 2017, ARep, 61, 406
Sand, K. R., Faber, J. T., Gajjar, V., et al. 2022, ApJ, 932, 98
Scargle, J. D. 1982, ApJ, 263, 835
Scheuer, P. A. G. 1968, Natur, 218, 920
Scott, D. W. 2015, Multivariate Density Estimation: Theory, Practice, and Visualization (New York: Wiley)
Sheikh, S., Brown, G. C., MacTaggart, J., et al. 2024, ApJ, 976, 225
Smith, F. G., & Wright, N. C. 1985, MNRAS, 214, 97
Stinebring, D. R., & Condon, J. J. 1990, ApJ, 352, 207
Stinebring, D. R., Faison, M. D., & McKinnon, M. M. 1996, ApJ, 460, 460
Turner, J. E., Joshi, B. C., McLaughlin, M. A., & Stinebring, D. R. 2024a, ApJ, 961, 101
Turner, J. E., Lebron Medina, J. G., Zelensky, Z., et al. 2024b, ApJ, 977, 205
Turner, J. E., McLaughlin, M. A., Cordes, J. M., et al. 2021, ApJ, 917, 10
van Straten, W., & Bailes, M. 2011, PASA, 28, 1
Virtanen, P., Gommers, R., Oliphant, T. E., et al. 2020, NatMe, 17, 261
Wang, N., Manchester, R. N., Johnston, S., et al. 2005, MNRAS, 358, 270
Wang, N., Yan, Z., Manchester, R. N., & Wang, H. X. 2008, MNRAS, 385, 1393
Wang, P. F., Han, J. L., Han, L., et al. 2018, A&A, 618, A186
Wolszczan, A. 1983, MNRAS, 204, 591
Wolszczan, A., Bartel, N., & Sieber, W. 1981, MNRAS, 196, 473
Wolszczan, A., Hesse, K. H., & Sieber, W. 1974, A&A, 37, 285
Wu, Z., Verbiest, J. P. W., Main, R. A., et al. 2022, A&A, 663, A116